Choice of observation type affects Bayesian calibration of ice sheet model projections

Denis Felikson[1,2], Sophie Nowicki[3], Isabel Nias[4], Beata Csatho[3], Anton Schenk[3], Michael Croteau[5], and Bryant Loomis[5]

[1]Cryospheric Sciences Laboratory, NASA Goddard Space Flight Center, Greenbelt, MD, USA
[2]Goddard Earth Sciences Technology and Research Studies and Investigations II, Morgan State University, Baltimore, MD, USA
[3]Department of Geology, University at Buffalo, Buffalo, NY, USA
[4]School of Environmental Sciences, University of Liverpool, Liverpool, UK
[5]Geodesy and Geophysics Laboratory, NASA Goddard Space Flight Center, Greenbelt, MD, USA

Correspondence: Denis Felikson (denis.felikson@nasa.gov)

Abstract. Determining reliable probability distributions for ice sheet mass change over the coming century is critical to improving uncertainties in sea-level rise projections. Bayesian calibration, a method for constraining projection uncertainty using observations, has been previously applied to ice sheet projections but the impact of the chosen observation type on the calibrated posterior probability distributions has not been quantified. Here, we perform three separate Bayesian calibrations to
5   constrain uncertainty in Greenland Ice Sheet projections using observations of velocity change, dynamic thickness change, and mass change. Comparing the posterior probability distributions shows that the maximum a posteriori ice sheet mass change can differ by 130% for the particular model ensemble that we used, depending on the observation type used in the calibration. More importantly for risk-averse sea level planning, posterior probabilities of high-end mass change scenarios are highly sensitive to the observation selected for calibration. Finally, we show that using mass change observations alone may result in projections
10   that overestimate flow acceleration and underestimate dynamic thinning around the margin of the ice sheet.

1 Introduction

Probabilistic sea-level rise projections are critical for coastal decision making. Assessment Report 6 (AR6) from the Intergovernmental Panel on Climate Change has compiled probabilistic projections, with the contribution from the Greenland and Antarctic Ice Sheets being quantified, for the first time, by higher-order numerical ice sheet models (Fox-Kemper et al., 2021;
15   Nowicki et al., 2020; Goelzer et al., 2020; Seroussi et al., 2020). However, the probabilistic ice sheet projections put forth in AR6 are not conditioned on observations. Performing calibration of projection ensembles using observations allows for refinement of the uncertainties estimated from the ensemble. Additionally, obtaining appropriate probabilities of high-end scenarios is critical for risk-averse coastal planning (Hinkel et al., 2015). For these reasons, it is important to understand the impact that any calibration approach has on the resulting central estimates of the projections as well as on the uncertainties of high-end
20   sea-level rise scenarios.

One method for conditioning ice sheet projection probabilities on observations is Bayesian calibration. This approach assigns a score each model simulations within an ensemble, based on model-observation residuals. The scores are used to construct a likelihood, which is used to update the prior probability distributions of model parameters and model outputs (e.g., ice sheet mass change). In this Bayesian framework, the "calibrated" probability distribution is also referred to as the posterior

25 probability distribution. Past studies have used this method to calibrate the relationship between surface mass balance and ice sheet surface elevation change (Edwards et al., 2014). Bayesian calibration has been used to constrain Antarctic Ice Sheet (AIS) mass change projections using satellite observations (Ritz et al., 2015) and using paleo observations (Gilford et al., 2020). The Bayesian calibration framework has been used to explore specific processes, such as the marine ice cliff instability (MICI), in terms of the impact of excluding MICI from AIS projections (Ruckert et al., 2017), as well as identifying the observational

30 constraints that are needed to assess the likelihood that MICI is occurring (Edwards et al., 2019). The aforementioned studies used observations of ice sheet mass change for calibration, however other observations have also been used. Surface elevation change rates were used to calibrate regional projections of mass change and grounding line retreat in Antarctica (Nias et al., 2019). There has also been recent work that has used a two-step calibration approach, first using observed ice sheet surface velocity and then using reconciled ice-sheet-wide mass change observations from the Ice Sheet Mass Balance Intercomparison

35 Experiment (The IMBIE team, 2018) to calibrate Greenland Ice Sheet mass change projections (Aschwanden and Brinkerhoff, 2022). The use of mass change observations to calibrate ice sheet model ensembles has been proposed as the logical path forward for creating credible sea-level change projections (Aschwanden et al., 2021). However, several different types of observations can be used to calibrate ice sheet projections and there has not yet been a study to systematically quantify the impact of the choice of observation type on the results of the calibration.

40 In this study, we explore the effect of different observation types on Bayesian calibration by using velocity change, thickness change, and mass change observations to perform separate calibrations of a Greenland Ice Sheet (GrIS) ensemble, which simulates Greenland's committed contribution to future sea-level change. Our study builds upon the work of Nias et al. (*in review*), which presents calibrated projections of this same ice sheet model ensemble using mass change observations. Here, we use the same calibration approach but perform additional calibrations using observed velocity and thickness changes and

45 compare the results from all three calibrations. Our focus in this study is on how the choice of observation type affects the posterior probability distributions of (1) ice sheet mass change and (2) model parameters and forcings that result from the calibration. We make an effort to be as consistent as possible in the setup of each of the three calibrations, in order to achieve a straightforward comparison. We describe the ice sheet model ensemble in Section 2.1 and the observations in Section 2.2. Results are presented in Section 4 and a discussion in Section 5.

50 ## 2 Data

2.1 Ice sheet model ensemble

We use an ensemble of model simulations that project the committed contribution from the GrIS to sea level over the coming century. The committed contribution captures the mass change of the GrIS in response to current atmospheric and oceanic

forcings, independent of future atmospheric or climate warming. The committed response can be thought of as the change that

55 is already locked in to the ice sheet, which will play out over the coming century. We summarize the model ensemble here and details can be found in Nias et al. (*in review*). The ice sheet simulations are performed using the Ice-sheet and Sea-level System Model (ISSM; Larour et al., 2012). The simulations are initialized to the year 2007 by inverting for a basal friction coefficient field using surface topography from the Greenland Ice Mapping Project (GIMP; Howat et al., 2014), bed topography from BedMachine v3 (Morlighem et al., 2017; Morlighem, 2017), and surface velocity from Interferometric Synthetic Aperture

60 Radar (InSAR) satellite data (Joughin et al., 2015b), following the methods of Morlighem et al. (2010). From the initial state in 2007, an ensemble of 137 forward runs is performed for the time period 2007-2100 by using Latin hypercube sampling (McKay et al., 1979; Eglajs and Audze, 1977) of uncertainty in basal friction, ice viscosity, and surface mass balance. Basal friction is varied by applying a spatially constant factor sampled from a uniform distribution with bounds of $\pm50\%$ to the field obtained from the inversion procedure, and this field is kept fixed through time. Ice viscosity is varied by applying a

65 spatially constant offset sampled from a uniform distribution with bounds of ±10 K to the initial temperature field, which is then converted to ice viscosity (Cuffey and Paterson, 2010), and this field is kept fixed through time. The surface mass balance (SMB) field is varied by (1) adding an offset and (2) changing the seasonal amplitude of the mean 2001-2015 SMB from the Regional Atmospheric Climate Model (RACMO2.3p2; Noël et al., 2019). The SMB offset is varied by applying a spatially constant factor sampled from a uniform distribution with bounds of $\pm30\%$ and the seasonal amplitude is varied by applying a

70 spatially constant factor sampled from a uniform distribution with bounds of 0 to 2, where a factor of 2 represents a doubling of the seasonal amplitude of SMB and a factor of 0 represents elimination of the seasonal amplitude. The variations in SMB offset and seasonal amplitude are applied spatially uniformly across the entire ice sheet and the annual SMB pattern is repeated yearly. From 2007 to 2015, the ice front in the model is specified using observations of outlet glacier terminus positions (Moon and Joughin, 2008; Joughin et al., 2015a) via a level-set method (Bondzio et al., 2016). From 2015 onward, the terminus

75 positions are held fixed in their 2015 locations, allowing the ice sheet to adjust to the 2007-2015 terminus perturbations and, thus, yielding the committed contribution from the GrIS, independent of future terminus position change.

2.2 Observations

2.2.1 Velocity change

The first observation type that we use for calibration is velocity change. Velocity change observations are computed using the

80 Making Earth System Data Records for Use in Research Environments (MEaSUREs) Greenland Ice Sheet Velocity Map from Interferometric Synthetic Aperture Radar (InSAR) Data, Version 2 (Joughin et al., 2015b). This dataset uses several sources of InSAR measurements to compile winter ice-sheet-wide velocity maps on an annual basis. We use the maps from 2007 and 2015 to obtain velocity change over these years. We calculate velocity change as the difference between the 2015 and 2007 velocity maps and uncertainty is calculated as the root sum of squares of the two associated uncertainty maps.

2.2.2 Dynamic thickness change

85

The second observation type that we use for calibration is dynamic thickness change. This quantity is a useful measure of how out of balance the ice dynamics are with the climate and, thus, it is a good metric for evaluating the ensemble. Ice sheet surface elevation change time series are obtained from airborne and spaceborne laser altimetry using the Surface Elevation Reconstruction and Change (SERAC) method (Schenk and Csatho, 2012; Shekhar et al., 2020). To obtain dynamic surface

90 elevation change, we account for thickness change anomalies due to surface and firn processes by applying the Institute for Marine and Atmospheric research Utrech (IMAU) Firn Densification Model (FDM), which simulates thickness change of the firn, forced by RACMO2.3p2 (Ligtenberg et al., 2018). We subtract the firn thickness change anomalies from the SERAC surface elevation change, with anomalies referenced to the average over the time period 1960-1979. We then fit a continuous function to the discrete SERAC estimates through time. Time series with a magnitude of dynamic thickness change greater

95 than 5 m over the entire SERAC time series are typically characterized by complex temporal behavior; at these locations, we use the Approximation by Localized Penalized Spline (ALPS) method (Shekhar et al., 2020) to approximate a continuous function through time. Time series with a magnitude of dynamic thickness change less than 5 m over the entire SERAC time series exhibit less complex behavior and we fit a cubic polynomial to the discrete SERAC estimates at these locations.

We sum the annual dynamic thickness change over the time period 2007-2015, only considering those SERAC locations that

100 have an estimate for each year between 2007 and 2015. This results in a set of more than 16,000 data points over the ice sheet in irregularly distributed locations, with higher density around the ice sheet margin where airborne altimetry provides increased spatial sampling beyond the spaceborne altimetry (Csatho et al., 2014). We assume that the dynamic surface elevation change from SERAC is equivalent to the dynamic thickness change because glacial isostatic adjustment rates around the margin of the GrIS are orders of magnitude smaller than the dynamic surface elevation change rate signal (Wake et al., 2016). As a final

105 step, we transform the coordinates of the dynamic thickness change time series locations from Universal Transverse Mercator (UTM) zone 24N (epsg:32624) to polar stereographic north (epsg:3413).

To assign uncertainties, we combine the approximation errors of ice thickness change from the ALPS and polynomial fits and inflate them to account for errors in the FDM and SMB estimates. We investigate fit errors from ALPS at locations where the magnitude of dynamic thickness change is > 5 m and find errors to be ∼1 m over the calibration time span. Similarly,

110 fit errors from the cubic polynomial at locations where the magnitude of dynamic thickness change is <5 m are ∼0.1 m. We conservatively inflate these to account for uncertainty in the SMB and FDM and use 1.4 m and 0.14 m as the uncertainties on dynamic thickness change where dynamic thickness change is >5 m and < 5 m, respectively. This achieves an expected spatial pattern in uncertainties, with larger uncertainties around the GrIS margin, where dynamic thickness change is relatively large, and smaller uncertainties in the GrIS interior, where dynamic thickness change is relatively small (Fig. 1).

2.2.3 Mass change

115

The third observation type we use for calibration is mass change observations. Mass change observations of the GrIS are derived from the high-spatial-resolution NASA Goddard Space Flight Center (GSFC) global mascon trend solution (release

06), obtained from the Gravity Recovery and Climate Experiment (GRACE) and the Gravity Recovery and Climate Experiment

Follow On (GRACE-FO) (Loomis et al., 2021). These observations provide mass change trends within 1-arc-degree equal area

120   cells, globally. Mass change over the calibration time span of 2007 – 2015 is calculated from the observed trends per mascon

over the GrIS. Mass change uncertainties are calculated from statistics of the differences between the GSFC high-spatial-

resolution mascon trend solution (Loomis et al., 2019) and the Gravity Observation Combination release 06 (GOCO-06)

spherical harmonic model (Kvas et al., 2021). The mass change uncertainties were assessed separately over the margin and

the interior of the GrIS and the resulting uncertainties are 4 cm w.e. yr^{-1} for the mascons around the GrIS margin and and 1

125   cm w.e. yr^{-1} for the mascons in the GrIS interior (Fig. 1). This results in a spatial pattern of mass change uncertainties that is

similar to that for dynamic thickness change, with relatively higher uncertainties around the GrIS margin and relatively lower

uncertainties in the GrIS interior.

3 Methods

3.1 Observation preprocessing

130   In our Bayesian calibration approach (described in Section 3.3), we assume that the model-observation residuals are indepen-

dent from one another. In other words, we assume no spatial correlation between residuals. In order to use this assumption

for velocity and thickness change, we coarsen the input observation datasets by establishing a regular polar stereographic grid

with 50 km by 50 km grid cells and calculating the mean observed quantity and uncertainty in each grid cell. Additionally, we

discard gridded velocity change observations for grid cells with less than 75% coverage. The mass change observations are ag-

135   gregated at a drainage basin scale, which are assumed to be spatially uncorrelated (Nias et al., *in review*). Gridded observations

and their uncertainties are shown in Figure 1.

3.2 Model output preprocessing

To calculate model-observation residuals, we must calculate model quantities that match the observed quantities. Velocity is

a model state variable and we can compare modeled velocity change directly with observations. Modeled dynamic thickness

140   change is calculated by subtracting the SMB anomaly (in units of ice thickness equivalent) from the modeled ice thickness

change over 2007–2015. SMB anomaly is calculated by subtracting the mean 1960-1979 SMB from the prescribed SMB forc-

ing for each simulation in the ensemble. The prescribed SMB forcing for the model simulations is obtained from RACMO2.3p2

(Noël et al., 2019) and the mean 1960-1979 SMB is calculated from this same model dataset. Our calculation of modeled dy-

namic thickness change corresponds to the method used to calculate observed dynamic thickness change, which uses an FDM

145   to estimate the thickness change associated with surface and firn processes and removes this from the observed surface eleva-

tion change to obtain dynamic ice thickness change. Modeled mass change is calculated by multiplying the modeled volume

change, which is also a model state variable, by a constant ice density (917 kg/m^3) to obtain mass change. Modeled mass

change is defined at the resolution of model elements and this is then converted to GRACE mascon space using the GRACE
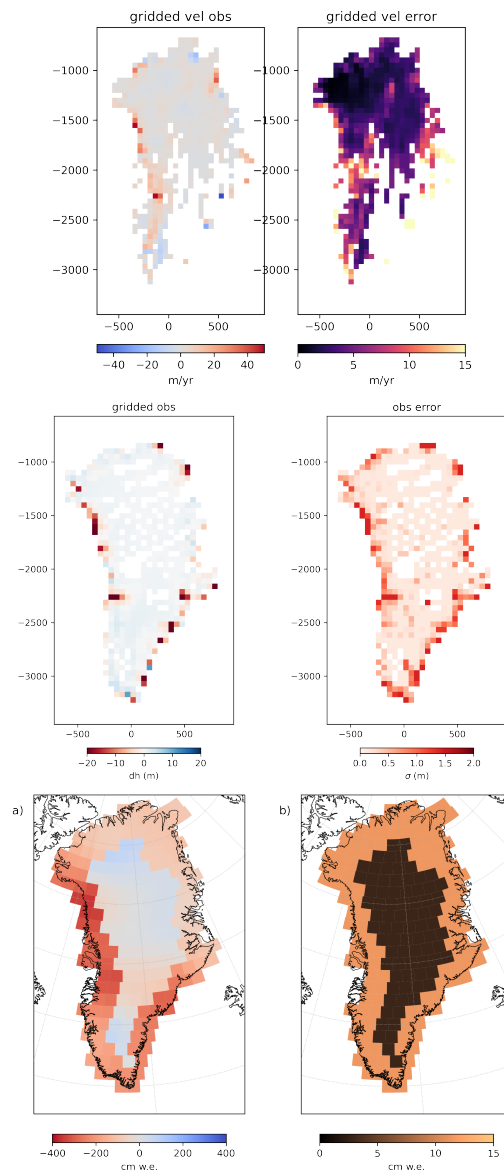
Figure 1. Gridded observations. Velocity change (a) and velocity change uncertainty (b), dynamic thickness change (c) and dynamic thickness change uncertainty (d), mass change (e) and mass change uncertainty (f) are shown.

resolution operator. Details on this conversion can be found in Nias et al. (*in review*) and the resolution operator is described
in (Loomis et al., 2019).

The modeled quantities are regridded spatially to match the observational quantities. Mean modeled velocity change and
dynamic thickness change are calculated within the grid cells defined by the same 50 km by 50 km grid used for the observational datasets. Modeled mass change is aggregated within the same drainage basins as used for aggregating the observed mass
change (Nias et al., *in review*).

3.3 Bayesian calibration

We use a Bayesian calibration approach to refine the spread in GrIS mass change projections and the uncertainty in model
parameters and forcings from our ice sheet model ensemble. In this approach, we calibrate the prior probability distributions
of (1) ice sheet mass change and (2) model parameters and forcings using observations of the ice sheet to obtain posterior
probability distributions of these quantities. Bayes' theorem states that:

$$p(\mathbf{m}|\mathbf{d}) \propto p(\mathbf{m})p(\mathbf{d}|\mathbf{m}) \tag{1}$$

where $p(\mathbf{m})$ is the prior probability distribution of model parameters, forcings, and the resulting mass change, $\mathbf{m}$, $p(\mathbf{d}|\mathbf{m})$ is
the likelihood function of $\mathbf{m}$ given observations, $\mathbf{d}$, and $p(\mathbf{m}|\mathbf{d})$ is the posterior probability distribution of $\mathbf{m}$.

To construct the likelihood, we use model-observation residuals to assign a likelihood score for each ensemble member. The
score for the jth ensemble member is calculated as:

$$s_j = \exp\left[-\frac{1}{2}\sum_i \frac{(f_i^j - z_i^j)^2}{(\sigma_i)^2}\right] \tag{2}$$

where f is the modeled quantity, z is the observed quantity, σ^2 is the variance of the residual, and i is a spatial index. For
the velocity and thickness change calibrations, the spatial index, i, represents each 50 km by 50 km grid cell within which
observations are defined and for the mass change calibration, the spatial index represents each basin within which mass change
observations are aggregated. Uncertainty in the residual includes both the observational uncertainty, σ_o, and the model (also
called structural) uncertainty, σ_m:

$$\sigma_i = \sqrt{\sigma_{o,i}^2 + \sigma_{m,i}^2} \tag{3}$$

Values for $\sigma_{m,i}$, are typically specified in an ad-hoc manner as a multiple of $\sigma_{o,i}$ (e.g., Edwards et al., 2014; Nias et al.,
2019). Here, we set $\sigma_{m,i} = k\sigma_{o,i}$ and we manually adjust k for each observation type such that the peaks of the posterior
probability distributions of GrIS committed contribution to global mean sea level (GMSL) in 2100 from our three calibrations
are approximately equal (Fig. 2). This choice allows us to compare the calibration results in a straightforward manner. The
multiplier, k, varies for each observation type and the values that we use are shown in Table 1.

Once the scores, s_j, are calculated for each calibration, they are normalized such that $\sum_{j=1}^{n} s_j = 1$, where n is the total
number of ensemble members, resulting in weights that are applied to the prior distributions of (1) mass change and (2) model
parameters and forcings to obtain the posterior distributions.

Table 1. Values for the multiplier, k, used to calculate structural model uncertainty from observational uncertainty.

Observation type	k
Velocity change	150
Thickness change	75
Mass change	8

180   We perform three separate calibrations using observations of (1) velocity, (2) thickness, or (3) mass change and compare the posterior probability distributions of GrIS committed contribution to GMSL in 2100, as well as model parameters and forcings, obtained from all three calibrations.

4   Results

The calibrated posterior probability distributions of GrIS committed contribution to GMSL and the associated statistics differ
185   between the three calibrations (Fig. 2, Table 2). The median and maximum a posteriori (MAP) GMSL vary significantly, based on the type of observation chosen for calibration. The MAP GMSL from the thickness change calibration is -10.3 mm, whereas the MAP GMSL from the mass change calibration is 35.1 mm, a difference of 130% of the MAP GMSL from the mass change calibration. As shown by the 95th percentile of the posterior distribution, all three calibrations decrease the probability of the highest possible contributions to GMSL; the prior probability distribution of GMSL has a 95th percentile of 213.3 mm and the
190   calibrations decrease this to <=77.8 mm (Table 2). The 5th percentiles are all negative, indicating that all three calibrations result in a possibility that Greenland will accumulate mass, decreasing GMSL. Like the 95th percentiles, the 5th percentiles also decrease in magnitude as a result of the calibration from -60.3 mm down to -14.7 mm for the mass change calibration. In other words, all three calibrations serve to narrow the probability distribution of the committed contribution to GMSL from the GrIS. The choice of observation type also has a strong effect on the cumulative probability of high-end scenarios (GMSL
195   >50 mm). Calibration using thickness change observations yields a 14.2% probability of GMSL >50 mm, whereas calibration using mass change observations yields a 28.1% probability of GMSL >50 mm, a 2-fold difference in probabilities. All three calibrations reduce the probability for the most extreme scenario (GMSL >100 mm) from 23% to <=0.6%.

Posterior probability distributions of model parameters and forcings for all three calibrations are shown in Fig. 3. In all cases, the extreme values of all parameters and forcings are de-weighted and the peaks of the posterior distributions occur
200   near the central values. The posterior distributions we obtain from the three calibrations are similar for ice temperature, and SMB seasonal amplitude. However, for the basal friction multiplier, there are notable differences in the posterior probability distributions between the three calibrations. Calibration using thickness change observations results in a posterior probability distribution that is skewed towards higher values of the basal friction multiplier, whereas the velocity change and mass change calibrations result in posterior probability distributions that are more symmetric. Similarly, for SMB mean shift, the thickness
205   change calibration results in higher probabilities of positive shifts than the velocity and mass change calibrations.
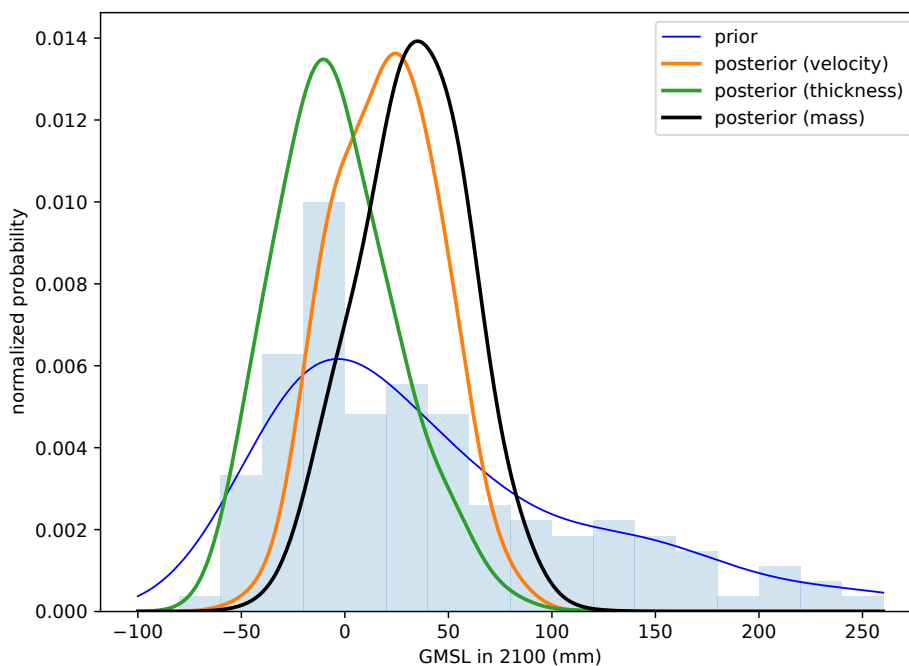
Figure 2. Posterior probability distributions of Greenland's committed contribution to global mean sea level (GMSL) in 2100 from three Bayesian calibrations: velocity (orange), thickness (green) and mass (black) change observations. Prior distribution shown as a blue curve and the histogram of the prior population is shown as a blue bar graph. Note that the y-axes are normalized probabilities, such that the integrals under the prior histograms and the posterior probability curves equals 1.

Table 2. Posterior probability statistics for GMSL in 2100: maximum a posteriori (MAP) (mm), median (mm), 5% and 95% percentiles (mm), and probability of GMSL larger than 50 and 100 mm (**P**(GMSL>50 mm) and **P**(GMSL>100 mm), respectively).

Calibration	MAP	median	Percentiles		**P**(GMSL>50 mm)	**P**(GMSL>100 mm)
			5%	95%		
Prior	-3.4	26.6	-60.3	213.3	38.8%	23.0%
Velocity	24.5	20.4	-23.9	64.5	14.2%	0.1%
Thickness	-10.3	-6.4	-51.0	51.2	5.3%	0.1%
Mass	35.1	33.8	-14.7	77.8	28.1%	0.6%

The three calibrations assign the heighest score to three different ensemble members with residuals revealing distinct spatial patterns (Fig. 4). All three calibrations result in larger residuals around the margin than in the interior of the ice sheet. Residuals for the same observational quantity used in each calibration are smaller than residuals from the other calibrations (Fig. 4a, e, i). In other words, velocity change residuals are smallest for the highest-weighted ensemble member from the velocity calibration and similarly for the thickness and mass change calibrations. Looking at velocity change residuals, all calibrations
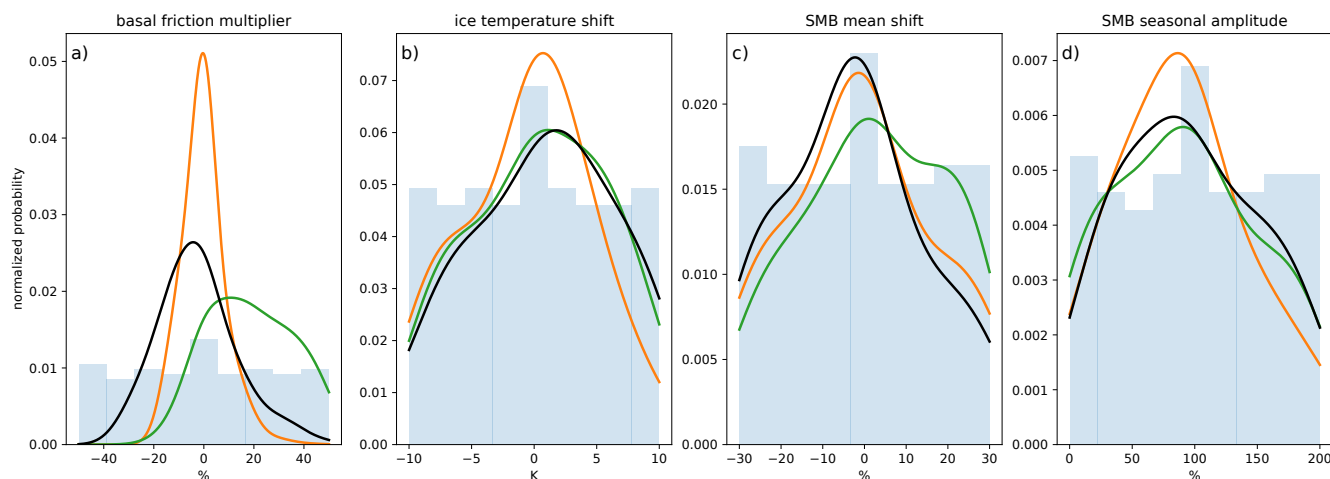
Figure 3. Prior and posterior probability distributions of model parameters and forcings: basal friction multiplier (a), ice temperature shift (b), SMB mean shift (c), and SMB seasonal amplitude (d). Prior probability distribution is shown as a histogram (light blue bars) and as a Gaussian approximation (blue curve). Posterior probabilities are shown for Bayesian calibrations using ice sheet surface velocity (orange), ice sheet thickness change (green), and ice sheet mass change (black). Note that the y-axes are normalized probabilities, such that the integrals under the prior histograms and the posterior probability curves equals 1.

overestimate velocity change along the eastern margin of the ice sheet and underestimate velocity change along the northern margin (Fig. 4a-c). Along the western margin, the residuals differ across the three calibrations, with the heighest-weighted ensemble member from the thickness calibration showing a large underestimate of velocity change (Fig. 4b). For outlet glaciers that have accelerated during the 2007-2015 calibration time period, this means that the acceleration is underestimated by the

215 thickness change calibration. The velocity change and mass change calibrations yield heighest-weighted ensemble members with a slight underestimate and slight overestimate of velocity change along the western margin, respectively (Fig. 4a and c). The thickness change residuals are similar in their spatial structure across all three calibrations (Fig. 4d-f). Dynamic thickness change residuals are positive around almost the entire margin of the ice sheet, meaning that the model underestimates the magnitude of observed dynamic thinning. The exception is the highest-weighted ensemble member from the thickness change

220 calibration, which underestimates thickness change around Jakobshavn Isbræ. The mass change residuals also have similar features across the three calibrations (Fig. 4g-i). Mass change residuals are positive in the east, southwest, and north, meaning the model underestimates the magnitude of observed mass loss in those regions. In the northeast, mass change residuals are negative, meaning the model overestimates the magnitude of observed mass loss there. In the northwest, there is a mix of positive and negative mass change residuals. Using the residuals' root sum of squares (RSS) as a measure, the velocity change

225 residuals show the highest sensitivity to the calibration choice, with a 38% difference in residuals' RSS between the velocity and thickness change calibrations. The thickness change and mass change residuals have less sensitivity, with a 16% difference
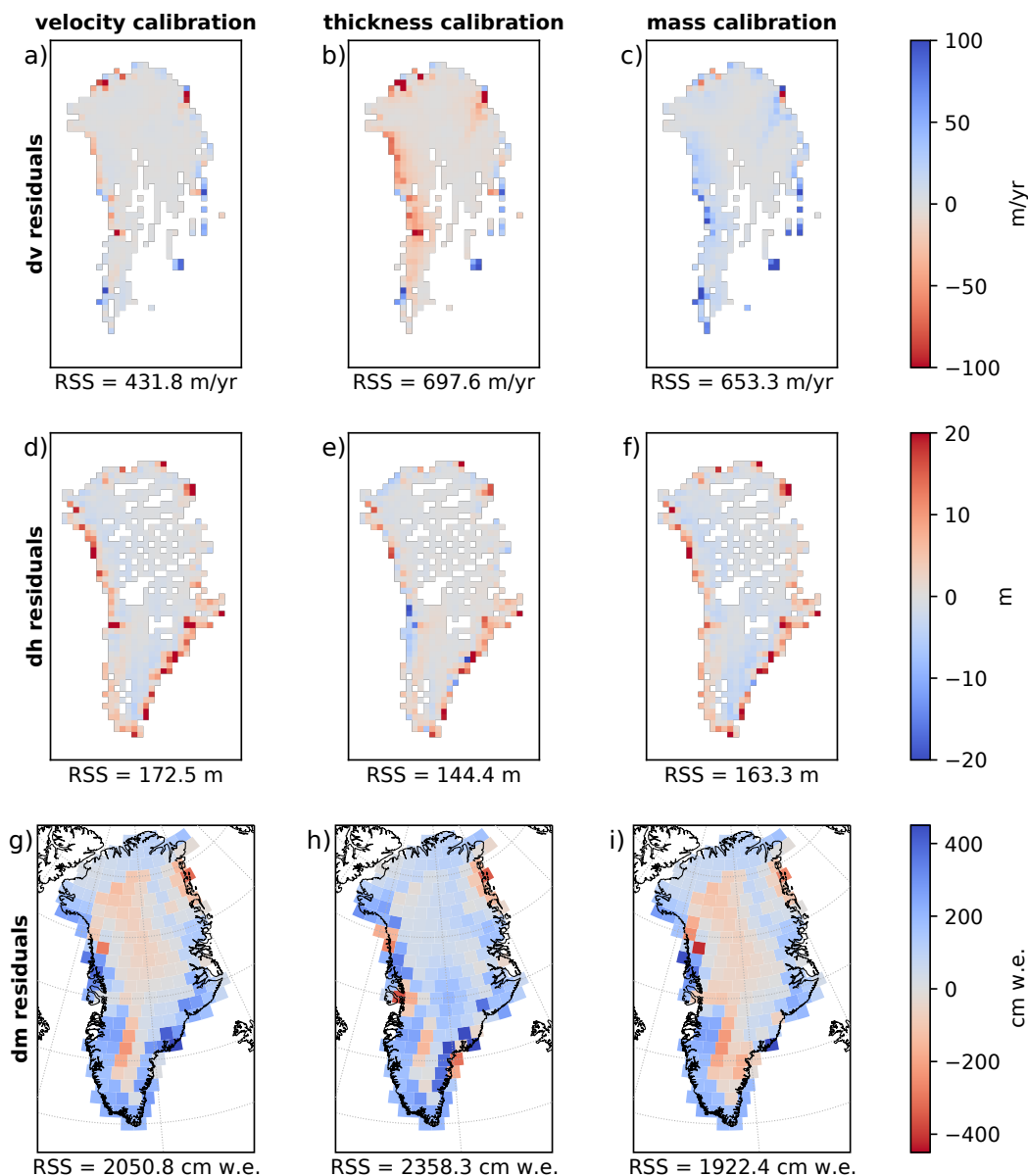
Figure 4. Residuals (modeled minus observed) for the highest weighted ensemble members from Bayesian calibration using velocity change (column 1), thickness change (column 2), and mass change (column 3) observations. Residuals of velocity (row 1), thickness (row 2), and mass (row 3) change over the calibration time period of 2007-2015 are shown.

in thickness change residuals' RSS between the velocity and thickness calibrations and an 18% difference in mass change residuals' RSS between the mass and thickness calibrations.

5 Discussion

230 The choice of observation type strongly affects the results of the calibration. This choice affects the posterior probability distributions of GrIS committed contribution to GMSL in 2100 (Fig. 2), as well as the posterior probability distributions of model parameters and forcings (Fig. 3). The maximum a posteriori estimate of GMSL in 2100 can differ by 130% (Table 2) and, more importantly, the probabilities of "high-end" scenarios can be very different, depending on the observation type used in the calibration. The posterior probability of >50 mm of committed GMSL in 2100 is a factor of 2 times larger for the

235 calibration using mass change than the calibration using thickness change observations (Table 2). The "highest-end" scenarios, however, are not sensitive to the choice of observation; all three calibrations effectively rule out the possibility of >100 mm of GMSL, regardless of the observation type, essentially eliminating the 23% cumulative probability of GMSL >100 mm in the prior distribution. The lower probability of a high-end scenario in the thickness change calibration is caused by the thickness change calibration assigning higher weights to ensemble members with higher basal friction coefficients and a higher SMB

240 mean shift (Fig. 3a and c, respectively).

Calibration using dynamic thickness change results in a posterior probability distribution of GrIS committed contribution to GMSL in 2100 that is quite different from the velocity change and mass change calibrations. Although the spread in the posterior probability distributions of GMSL in 2100 is similar across the three calibrations, as seen from the percentiles in Table 2, the MAP and median estimates from the thickness change calibration (-10 mm and -6 mm, respectively) are negative,

245 indicating that the GrIS is increasing in mass, whereas the MAP and estimates from the velocity change and mass change calibrations are positive, indicating that the GrIS is decreasing in mass. This corresponds with the thickness change calibration assigning higher likelihood to simulations with higher basal friction and a positive shift in mean SMB than the velocity and mass change calibrations (Fig. 3a and c, respectively). Simulations with higher basal friction result in a slower propagation of mass loss into the interior of the ice sheet in response to terminus retreat (Nias et al., *in review*) and this can be seen in

250 the larger negative velocity change residuals that extend further into the ice sheet interior for the highest-weighted ensemble member from the thickness calibration, indicating that ice sheet acceleration is underestimated by the model (Fig. 4b).

One potential source for a bias in the thickness change calibration is the firn thickness change modeling. An FDM is used to account for firn thickness change and to obtain dynamic ice thickness change from observations of surface elevation change. The ice sheet model does not simulate firn processes and, thus, a bias in the firn thickness change, caused by either a bias in the

255 trend during the 1960-1979 baseline time period or a during the 2007-2015 calibration time period, will have a direct effect on the calibration of GMSL. For example, a bias in firn thickness change of 10 cm/yr in the ice sheet interior, making observed dynamic thickness change 80 cm lower over the 2007–2015 calibration time period, shifts the median posterior GMSL from -6 mm to +7 mm (Section S1, Table S1, and Fig. S1 in Supplementary Materials), bringing it more in line with the medians from the velocity and mass change calibrations. Future work should focus on investigating the magnitude and sources of possible

260 biases in firn thickness change, as well as the spatial structure in these potential biases, which will improve the calibration of GrIS projections using thickness change observations.

Differences among the three calibrations in terms of their residuals can provide insight into biases in the model ensemble beyond what can be gleaned from any one of the calibrations alone. For example, the highest-weighted ensemble member from the mass change ensemble overestimates acceleration (Fig. 4c) and underestimates dynamic thinning along almost the entirety of the GrIS margin (Fig. 4f). The velocity calibration calculates the heighest weight for an ensemble member that better reproduces observed velocity change (Fig. 4a) but it should be noted that ice sheet velocity observations from 2007 are used in the initialization of the model (Nias et al., *in review*). Thus, care must be taken when interpreting the results of the calibration because the velocity change observations are not independent of the modeled velocities. One way to build on our results is to produce one calibration that uses all three observation types together, accounting for the uncertainties of each observation type. Aschwanden and Brinkerhoff (2022) have taken a step in this direction, by performing a two-step calibration process of GrIS projections, first using observations of velocity to calibrate a subset of model parameters and second using observations of mass change to calibrate the rest of the parameters. This is a notable advancement in utilizing information from multiple observations for Bayesian calibration. However, open question still remain. The first calibration step in Aschwanden and Brinkerhoff (2022) uses observed velocity rather than observed velocity change. This may potentially explain the discrepancy between their posterior modeled median ice sheet discharge, which remains constant through time, and the observed discharge, which is increasing over time (see Fig. 4a in Aschwanden and Brinkerhoff (2022)). Additionally, the second step of calibration using mass change in Aschwanden and Brinkerhoff (2022) does not shift the posterior median estimate of ice sheet mass change but does reduce the width of the posterior distribution. Their approach did not take model structural uncertainty into account and differences in the structural uncertainty between the different observation types will directly affect the widths of the resulting posterior distributions. More work needs to be done to better understand the structural model uncertainty for the different observation types and how to appropriately assign this to produce a combined calibration using all observation types.

Basal friction is the most sensitive parameter to choice in observation type (Fig. 3a). The velocity change calibration yields a posterior distribution that has a higher peak and narrower spread for basal friction than the other two calibrations. Posteriors for the other parameters and forcings (ice temperature, mean SMB, and seasonal SMB) are less sensitive to on the choice of observation used in the calibration. The narrower posterior distribution of basal friction from the velocity change calibration also corresponds to a slightly narrower posterior probability distribution of GMSL in 2100 from that calibration (Fig. 2), as shown by the percentiles in Table 2.

Our approach for specifying the structural model uncertainty, σ_m, significantly inflates the total uncertainty in the residuals, σ. To specify the structural uncertainty, we use a multiplier to scale the uncertainty in each observation type. The multipliers are 150 and 75 for velocity and thickness change uncertainty, respectively, meaning that the structural model uncertainty is 2 orders of magnitude larger than the observation uncertainty on velocity and thickness change. When the structural uncertainty is adjusted in an ad-hoc manner, as we have done, it is more critical to correctly specify the relative values of observation uncertainty than it is to specify the absolute values. In other words, it is more important to correctly specify the spatial pattern in observation uncertainty than it is to obtain a good estimate of the actual uncertainty values.

Data limitations may be contributing to differences between the three calibrations. The most obvious data limitation is the missing velocity change data in southeast Greenland, caused by data gaps in the 2007 velocity observations. This gap

in the observational data means that the model simulations are not scored based on their ability to capture velocity change in southeast Greenland. In contrast, the thickness change and mass change observations provide adequate data coverage to sample the southeast of the GrIS. To fill the velocity data gap, a later start year could be selected for the calibration. However, selecting velocity observations from a later year will inevitably mean shortening the calibration timespan and, thus, potentially losing information in the likelihood. This tradeoff between filling data gaps in velocity observations but shortening the calibration timespan should be explored in future work.

For our study, we used an ensemble of GrIS committed contribution to GMSL, which quantifies the changes that are locked in to the ice sheet, independent of any additional future atmospheric or oceanic forcing. Greenland's commitment results in contributions to GMSL that are similar in magnitude to the contribution due to future climate anomalies under the RCP2.6 and SSP1-26 scenarios (Edwards et al., 2021) but lower in magnitude than the contributions under the higher emissions scenarios. Additional work is needed to perform similar Bayesian calibrations of GrIS ensembles forced with future climate anomaly projections (e.g., Goelzer et al., 2020; Aschwanden et al., 2019). However, we hypothesize that there will be significant discrepancies among the posterior distributions of GrIS contribution to GMSL in these ensembles, similar to what we have found for the ensemble used in our study.

6 Conclusions

Our study presents three calibrations using three different observation types (velocity, thickness, and mass change) of the ice sheet over an 8-year time period. The choice of observation type leads to important differences in the posterior probability distributions of GrIS committed contribution to GMSL in 2100. It has been proposed that mass change observations should be used to calibrate ice sheet model projections (Aschwanden et al., 2021). However, as we have shown, the mass change calibration does not necessarily mean that ensemble members with the highest likelihoods will reproduce certain desired behaviors, such as matching observed outlet glacier dynamic thinning or acceleration. In other words, using a single observation type, such as mass change, may lead to obtaining the right answer but for the wrong reason, such as an overestimate of glacier acceleration and an underestimate in glacier thinning, as was the case in our study. More work must be done to better understand the impact of various choices made during the calibration process and to develop better approaches to incorporating information from different observation types.

Using Bayesian calibration to constrain uncertainty in ice sheet projections still has many open questions. We have clearly shown how Bayesian calibration can refine uncertainties in ice sheet projections but future work should explore additional choices, such as the method for specifying model structural uncertainty, the timespan over which the calibration is done, the use of time series of observations rather than a snapshot of change, and the use of additional metrics derived from these observations. Additionally, future work can move away from the simplifying assumption that we have made that model-calibration residuals are uncorrelated and, instead, quantify the correlation and incorporate that through a covariance matrix into the calibration procedure. Ultimately, the question is how to make use of all of the observation types to get the best possible

calibration, although, as we have shown, utilizing different observation types in separate calibrations can yield additional insight
330 into biases in the model ensemble.

Code and data availability. Velocity observations from the Making Earth System Data Records for Use in Research Environments (MEa-SUREs) project are available at https://doi.org/10.5067/OC7B04ZM9G6Q. Mass change observations derived from the Gravity Recovery And Climate Experiment (GRACE) and Gravity Recovery And Climate Experiment - Follow-on (GRACE-FO) are available at https://earth.gsfc.nasa.gov/geo/data/grace-mascons. Code for Bayesian calibration is available at https://doi.org/10.5281/zenodo.7272642.

335 *Author contributions.* DF and SN conceptualized the study. IN designed the model ensemble and performed the mass change calibration. DF performed the velocity change and thickness change calibrations, and carried out the comparison of the results from the three calibrations. BC and AS prepared the thickness change observations. MC and BL prepared the mass change observations. DF prepared the manuscript with contributions from all co-authors.

Competing interests. The authors declare that they have no conflict of interest.

340 *Acknowledgements.* DF was supported by funding from the NASA Sea-Level Change Team (grant #NN-H19ZDA001N-SLCST) and the NASA New Investigators Program (grant #80NSSC21K1734). SN was supported by the NASA Sea-Level Change Team (grant #NN-H19ZDA001N-SLCST). MC and BL were supported by the NASA GRACE-FO Science Team (grant #NN-H19ZDA001N-GRACEFO) and the NASA Sea Level Change Team, (grant #NN-H19ZDA001N-SLCST.) BC and AF were supported by NASA Sea-Level Change Team (grant #80NSSC17K0611) and ICESat-2 Science Team (grant #80NSSC21K0915).

References

Aschwanden, A. and Brinkerhoff, D. J.: Calibrated Mass Loss Predictions for the Greenland Ice Sheet, Geophysical Research Letters, 49, e2022GL099 058, https://doi.org/10.1029/2022GL099058, 2022.

Aschwanden, A., Fahnestock, M. A., Truffer, M., Brinkerhoff, D. J., Hock, R., Khroulev, C., Mottram, R. H., and Khan, S. A.: Contribution of the Greenland Ice Sheet to Sea Level over the next Millennium, Science Advances, 5, https://doi.org/10.1126/sciadv.aav9396, 2019.

Aschwanden, A., Bartholomaus, T. C., Brinkerhoff, D. J., and Truffer, M.: Brief Communication: A Roadmap towards Credible Projections of Ice Sheet Contribution to Sea Level, The Cryosphere, 15, 5705–5715, https://doi.org/10.5194/tc-15-5705-2021, 2021.

Bondzio, J. H., Seroussi, H., Morlighem, M., Kleiner, T., Rückamp, M., Humbert, A., and Larour, E. Y.: Modelling Calving Front Dynamics Using a Level-Set Method: Application to Jakobshavn Isbræ, West Greenland, The Cryosphere, 10, 497–510, https://doi.org/10.5194/tc-10-497-2016, 2016.

Csatho, B. M., Schenk, A. F., van der Veen, C. J., Babonis, G., Duncan, K., Rezvanbehbahani, S., van den Broeke, M. R., Simonsen, S. B., Nagarajan, S., and van Angelen, J. H.: Laser Altimetry Reveals Complex Pattern of Greenland Ice Sheet Dynamics, Proceedings of the National Academy of Sciences, 111, 18 478–18 483, https://doi.org/10.1073/pnas.1411680112, 2014.

Cuffey, K. and Paterson, W. S. B.: The Physics of Glaciers, Academic Press, fourth edn., 2010.

Edwards, T. L., Fettweis, X., Gagliardini, O., Gillet-Chaulet, F., Goelzer, H., Gregory, J. M., Hoffman, M., Huybrechts, P., Payne, A. J., Perego, M., Price, S., Quiquet, A., and Ritz, C.: Probabilistic Parameterisation of the Surface Mass Balance–Elevation Feedback in Regional Climate Model Simulations of the Greenland Ice Sheet, The Cryosphere, 8, 181–194, https://doi.org/10.5194/tc-8-181-2014, 2014.

Edwards, T. L., Brandon, M. A., Durand, G., Edwards, N. R., Golledge, N. R., Holden, P. B., Nias, I. J., Payne, A. J., Ritz, C., and Wernecke, A.: Revisiting Antarctic Ice Loss Due to Marine Ice-Cliff Instability, Nature, 566, 58–64, https://doi.org/10.1038/s41586-019-0901-4, 2019.

Edwards, T. L., Nowicki, S., Marzeion, B., Hock, R., Goelzer, H., Seroussi, H., Jourdain, N. C., Slater, D. A., Turner, F. E., Smith, C. J., McKenna, C. M., Simon, E., Abe-Ouchi, A., Gregory, J. M., Larour, E., Lipscomb, W. H., Payne, A. J., Shepherd, A. P., Agosta, C., Alexander, P., Albrecht, T., Anderson, B., Asay-Davis, X., Aschwanden, A., Barthel, A., Bliss, A., Calov, R., Chambers, C., Champollion, N., Choi, Y., Cullather, R., Cuzzone, J., Dumas, C., Felikson, D., Fettweis, X., Fujita, K., Galton-Fenzi, B. K., Gladstone, R., Golledge, N. R., Greve, R., Hattermann, T., Hoffman, M. J., Humbert, A., Huss, M., Huybrechts, P., Immerzeel, W., Kleiner, T., Kraaijenbrink, P., clec'h, S., Lee, V., Leguy, G. R., Little, C. M., Lowry, D. P., Malles, J.-H., Martin, D. F., Maussion, F., Morlighem, M., O'Neill, J. F., Nias, I., Pattyn, F., Pelle, T., Price, S. F., Quiquet, A., Radić, V., Reese, R., Rounce, D. R., Rückamp, M., Sakai, A., Shafer, C., Schlegel, N.-J., Shannon, S., Smith, R. S., Straneo, F., Sun, S., Tarasov, L., Trusel, L. D., Breedam, J., Wal, R., Broeke, M., Winkelmann, R., Zekollari, H., Zhao, C., Zhang, T., and Zwinger, T.: Projected Land Ice Contributions to Twenty-First-Century Sea Level Rise, Nature, pp. 1–26, https://doi.org/10.1038/s41586-021-03302-y, 2021.

Eglajs, V. and Audze, P.: New Approach to the Design of Multifactor Experiments, Problems of Dynamics and Strengths, 35, 104–107, 1977.

Fox-Kemper, B., Hewitt, H., Xiao, C., Aðalgeirsdóttir, G., Drijfhout, S., Edwards, T., Golledge, N., Hemer, M., Kopp, R., Krinner, G., Mix, A., Notz, D., Nowicki, S., Nurhati, I., Ruiz, L., Sallée, J.-B., Slangen, A., and Yu, Y.: Ocean, Cryosphere and Sea Level Change, in: Climate Change 2021: The Physical Science Basis. Contribution of Working Group I to the Sixth Assessment Report of the Intergovernmental Panel on Climate Change, edited by Masson-Delmotte, V., Zhai, P., Pirani, A., Connors, S., Péan, C., Berger, S., Caud, N., Chen, Y.,

Goldfarb, L., Gomis, M., Huang, M., Leitzell, K., Lonnoy, E., Matthews, J., Maycock, T., Waterfield, T., Yelekçi, O., Yu, R., and Zhou, B., pp. 1211–1362, Cambridge University Press, Cambridge, United Kingdom and New York, NY, USA, 2021.

Gilford, D. M., Ashe, E. L., DeConto, R. M., Kopp, R. E., Pollard, D., and Rovere, A.: Could the Last Interglacial Constrain Projections of Future Antarctic Ice Mass Loss and Sea-Level Rise?, Journal of Geophysical Research: Earth Surface, 125, e2019JF005 418, https://doi.org/10.1029/2019JF005418, 2020.

Goelzer, H., Nowicki, S., Payne, A., Larour, E., Seroussi, H., Lipscomb, W. H., Gregory, J., Abe-Ouchi, A., Shepherd, A. P., Simon, E., Agosta, C., Alexander, P., Aschwanden, A., Barthel, A., Calov, R., Chambers, C., Choi, Y., Cuzzone, J., Dumas, C., Edwards, T., Felikson, D., Fettweis, X., Golledge, N. R., Greve, R., Humbert, A., Huybrechts, P., Le clec'h, S., Lee, V., Leguy, G., Little, C., Lowry, D. P., Morlighem, M., Nias, I., Quiquet, A., Rückamp, M., Schlegel, N.-J., Slater, D. A., Smith, R. S., Straneo, F., Tarasov, L., van de Wal, R., and van den Broeke, M. R.: The Future Sea-Level Contribution of the Greenland Ice Sheet: A Multi-Model Ensemble Study of ISMIP6, The Cryosphere, 14, 3071–3096, https://doi.org/10.5194/tc-14-3071-2020, 2020.

Hinkel, J., Jaeger, C., Nicholls, R. J., Lowe, J., Renn, O., and Peijun, S.: Sea-Level Rise Scenarios and Coastal Risk Management, Nature Climate Change, 5, 188–190, https://doi.org/10.1038/nclimate2505, 2015.

Howat, I. M., Negrete, A., and Smith, B. E.: The Greenland Ice Mapping Project (GIMP) Land Classification and Surface Elevation Data Sets, The Cryosphere, 8, 1509–1518, https://doi.org/10.5194/tc-8-1509-2014, 2014.

Joughin, I., Moon, T., Joughin, J., and Black, T.: MEaSUREs Annual Greenland Outlet Glacier Terminus Positions from SAR Mosaics, Version 1, https://doi.org/10.5067/DC0MLBOCL3EL, 2015a.

Joughin, I., Smith, B., Howat, I., and Scambos, T.: MEaSUREs Greenland Ice Sheet Velocity Map from InSAR Data, Version 2, https://doi.org/10.5067/OC7B04ZM9G6Q, 2015b.

Kvas, A., Brockmann, J. M., Krauss, S., Schubert, T., Gruber, T., Meyer, U., Mayer-Gürr, T., Schuh, W.-D., Jäggi, A., and Pail, R.: GOCO06s – a Satellite-Only Global Gravity Field Model, Earth System Science Data, 13, 99–118, https://doi.org/10.5194/essd-13-99-2021, 2021.

Larour, E. Y., Seroussi, H., Morlighem, M., and Rignot, E.: Continental Scale, High Order, High Spatial Resolution, Ice Sheet Modeling Using the Ice Sheet System Model (ISSM), Journal of Geophysical Research, 117, https://doi.org/10.1029/2011JF002140, 2012.

Ligtenberg, S. R. M., Kuipers Munneke, P., Noël, B. P. Y., and van den Broeke, M. R.: Brief Communication: Improved Simulation of the Present-Day Greenland Firn Layer (1960–2016), The Cryosphere, 12, 1643–1649, https://doi.org/10.5194/tc-12-1643-2018, 2018.

Loomis, B. D., Richey, A. S., Arendt, A. A., Appana, R., Deweese, Y.-J. C., Forman, B. A., Kumar, S. V., Sabaka, T. J., and Shean, D. E.: Water Storage Trends in High Mountain Asia, Frontiers in Earth Science, 7, 2019.

Loomis, B. D., Felikson, D., Sabaka, T. J., and Medley, B.: High-Spatial-Resolution Mass Rates From GRACE and GRACE-FO: Global and Ice Sheet Analyses, Journal of Geophysical Research: Solid Earth, 126, e2021JB023 024, https://doi.org/10.1029/2021JB023024, 2021.

McKay, M. D., Beckman, R. J., and Conover, W. J.: A Comparison of Three Methods for Selecting Values of Input Variables in the Analysis of Output from a Computer Code, Technometrics : a journal of statistics for the physical, chemical, and engineering sciences, 21, 239–245, 1979.

Moon, T. and Joughin, I. R.: Changes in Ice Front Position on Greenland's Outlet Glaciers from 1992 to 2007, Journal of Geophysical Research, 113, F02 022, https://doi.org/10.1029/2007JF000927, 2008.

Morlighem, M.: IceBridge BedMachine Greenland, Version 3, https://doi.org/10.5067/2CIX82HUV88Y, 2017.

Morlighem, M., Rignot, E., Seroussi, H., Larour, E. Y., Ben Dhia, H., and Aubry, D.: Spatial Patterns of Basal Drag Inferred Using Control Methods from a Full-Stokes and Simpler Models for Pine Island Glacier, West Antarctica, Geophysical Research Letters, 37, n/a–n/a, https://doi.org/10.1029/2010GL043853, 2010.

Morlighem, M., Williams, C. N., Rignot, E., An, L., Arndt, J. E., Bamber, J. L., Catania, G., Chauché, N., Dowdeswell, J. A., Dorschel,
420   B., Fenty, I., Hogan, K., Howat, I. M., Hubbard, A., Jakobsson, M., Jordan, T. M., Kjeldsen, K. K., Millan, R., Mayer, L., Mougi-
not, J., Noël, B. P. Y., O'Cofaigh, C., Palmer, S., Rysgaard, S., Seroussi, H., Siegert, M. J., Slabon, P., Straneo, F., van den Broeke,
M. R., Weinrebe, W., Wood, M., and Zinglersen, K. B.: BedMachine v3: Complete Bed Topography and Ocean Bathymetry Mapping
of Greenland from Multibeam Echo Sounding Combined with Mass Conservation, Geophysical Research Letters, 44, 11,051–11,061,
https://doi.org/10.1002/2017GL074954, 2017.

425   Nias, I. J., Cornford, S. L., Edwards, T. L., Gourmelen, N., and Payne, A. J.: Assessing Uncertainty in the Dynamical Ice Re-
sponse to Ocean Warming in the Amundsen Sea Embayment, West Antarctica, Geophysical Research Letters, 46, 11 253–11 260,
https://doi.org/10.1029/2019GL084941, 2019.

Noël, B. P. Y., van de Berg, W. J., Lharmitte, S., and van den Broeke, M. R.: Rapid Ablation Zone Expansion Amplifies North Greenland
Mass Loss, Science Advances, 5, 2019.

430   Nowicki, S., Goelzer, H., Seroussi, H., Payne, A. J., Lipscomb, W. H., Abe-Ouchi, A., Agosta, C., Alexander, P., Asay-Davis, X. S., Barthel,
A., Bracegirdle, T. J., Cullather, R., Felikson, D., Fettweis, X., Gregory, J. M., Hattermann, T., Jourdain, N. C., Kuipers Munneke, P.,
Larour, E., Little, C. M., Morlighem, M., Nias, I., Shepherd, A. P., Simon, E., Slater, D. A., Smith, R. S., Straneo, F., Trusel, L. D., van
den Broeke, M. R., and van de Wal, R.: Experimental Protocol for Sea Level Projections from ISMIP6 Stand-Alone Ice Sheet Models,
The Cryosphere, 14, 2331–2368, https://doi.org/10.5194/tc-14-2331-2020, 2020.

435   Ritz, C., Durand, G., Payne, A. J., Peyaud, V., Hindmarsh, R. C. A., and Edwards, T. L.: Potential Sea-Level Rise from Antarctic Ice-Sheet
Instability Constrained by Observations, Nature, 528, 115–118, https://doi.org/10.1038/nature16147, 2015.

Ruckert, K. L., Shaffer, G., Pollard, D., Guan, Y., Wong, T. E., Forest, C. E., and Keller, K.: Assessing the Impact of
Retreat Mechanisms in a Simple Antarctic Ice Sheet Model Using Bayesian Calibration, PLOS ONE, 12, e0170 052–15,
https://doi.org/10.1371/journal.pone.0170052, 2017.

440   Schenk, T. and Csatho, B. M.: A New Methodology for Detecting Ice Sheet Surface Elevation Changes from Laser Altimetry Data, IEEE
Transactions on Geoscience and Remote Sensing, 50, 3302–3316, https://doi.org/10.1109/tgrs.2011.2182357, 2012.

Seroussi, H., Nowicki, S., Payne, A. J., Goelzer, H., Lipscomb, W. H., Abe-Ouchi, A., Agosta, C., Albrecht, T., Asay-Davis, X., Barthel,
A., Calov, R., Cullather, R., Dumas, C., Galton-Fenzi, B. K., Gladstone, R., Golledge, N. R., Gregory, J. M., Greve, R., Hattermann, T.,
Hoffman, M. J., Humbert, A., Huybrechts, P., Jourdain, N. C., Kleiner, T., Larour, E., Leguy, G. R., Lowry, D. P., Little, C. M., Morlighem,
445   M., Pattyn, F., Pelle, T., Price, S. F., Quiquet, A., Reese, R., Schlegel, N.-J., Shepherd, A. P., Simon, E., Smith, R. S., Straneo, F., Sun, S.,
Trusel, L. D., Van Breedam, J., van de Wal, R. S. W., Winkelmann, R., Zhao, C., Zhang, T., and Zwinger, T.: ISMIP6 Antarctica: A Multi-
Model Ensemble of the Antarctic Ice Sheet Evolution over the 21st Century, The Cryosphere, 14, 3033–3070, https://doi.org/10.5194/tc-
14-3033-2020, 2020.

Shekhar, P., Csathó, B., Schenk, T., Roberts, C., and Patra, A. K.: ALPS: A Unified Framework for Modeling Time Series of Land Ice
450   Changes, IEEE Transactions on Geoscience and Remote Sensing, 59, 6466–6481, https://doi.org/10.1109/TGRS.2020.3027190, 2020.

The IMBIE team: Mass Balance of the Antarctic Ice Sheet from 1992 to 2017, Nature, 558, 219–222, https://doi.org/10.1038/s41586-018-
0179-y, 2018.

Wake, L. M., Lecavalier, B. S., and Bevis, M. G.: Glacial Isostatic Adjustment (GIA) in Greenland: A Review, Current Climate Change
Reports, 2, 101–111, https://doi.org/10.1007/s40641-016-0040-z, 2016.